Interferometric Imaging With Terahertz Pulses

Jon L. Johnson, Timothy D. Dorney, and Daniel M. Mittleman

***Abstract*—We demonstrate a new reflection imaging technique using single-cycle pulses, in which the sample to be imaged is placed at the focus of a lens in one arm of a Michelson interferometer. The detected signal is the superposition of the pulses from the two arms of the interferometer, one with a sample and one with a reference mirror. Because of the Gouy phase shift from the lens in the sample arm, these two pulses are nearly π out of phase, and can destructively interfere. This leads to a strong cancellation of the measured waveform and a nearly background-free imaging method. We demonstrate the technique using terahertz time-domain spectroscopy and show that the destructive interference provides enhanced sensitivity to features in the sample that are much thinner than the coherence length of the radiation. This technique could be valuable in any low-coherence tomographic measurement in which the reflected electric field can be measured directly.**

***Index Terms*—Gouy phase shift, interferometry, terahertz imaging, terahertz time-domain spectroscopy.**

IMAGING via time-of-flight tomography is common in many fields of research. Techniques such as optical coherence tomography (OCT) [1] have found widespread application, in part because of their ability to image with high depth resolution. In OCT, for example, this resolution is achieved by using a low-coherence light source, such as a femtosecond optical pulse [2]. In this case, the depth resolution is determined solely by the bandwidth of the light source. This is a manifestation of the well-known Rayleigh criterion, which relates the achievable depth resolution to the coherence length L_c, inversely proportional to the bandwidth [3]. Using broadband optical pulses of 10 fs duration, it is possible to resolve two reflecting surfaces spaced by only a few micrometers [4]. To achieve this extraordinary resolution, an interferometric arrangement is typically employed. This provides a synchronized reference pulse, which can act as a temporal gate.

We have recently described a time-of-flight reflection imaging technique using single-cycle pulses of terahertz (THz) radiation [5]. In this case, photoconductive sampling permits the direct detection of the THz electric field [6]. As a result, the temporal separation between pulses reflected from two closely separated surfaces can be determined directly from the time-domain waveform, without any need for interferometry. In this previous work, as in OCT, the depth resolution was determined by the Rayleigh criterion. Two surfaces can only be distinguished if the distance between them is larger than $L_c/2$. Here, the factor of 1/2 arises from the two transits through the intervening medium of the pulse reflected from the farther surface. A depth resolution of $\sim$100 μm was demonstrated using this simple time-of-flight imaging system [5]. It is important to note that it was possible to attain this Rayleigh-limited imaging without the use of interferometry, because of the coherent detection of the THz waveforms. With single-beam time-of-flight techniques such as this, the only way to improve the depth resolution is to increase the bandwidth of the radiation.

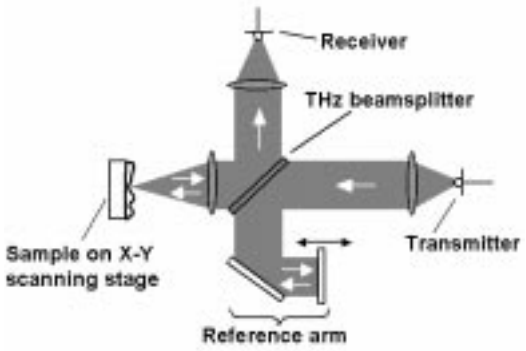

Fig. 1. A schematic of the experimental apparatus. The system is a THz time-domain spectrometer based on photoconductive antennas for both generation and detection. The collimated THz beam is divided into two by a high-resistivity silicon beam splitter, in a Michelson arrangement. One arm is directed onto the sample through a focusing lens. The second arm is a reference retro-reflector, mounted on a manual delay stage. The sample and reference arms are recombined at the beam splitter and interfere coherently at the detector. To form images, the sample is translated transverse to the THz beam propagation direction.

In this paper, we describe an imaging technique that exploits interferometry to enhance the capabilities of low-coherence tomography. Because an interferometer is not already required to provide temporal gating, it can be instead used to implement a background-free imaging method. This technique exploits the Gouy phase shift incurred by an optical beam passing through a focus [7]. Since this phase shift is approximately equal to π, it can be used to induce a destructive interference between two optical pulses. This provides a nearly background-free imaging mode and leads to a dramatic increase in the sensitivity to subtle features in a sample. The value of phase-sensitive interferometry has long been recognized as a method for improving the signal-to-noise ratio in spectroscopic measurements [8], [9] and in imaging [10], [11]. However, this is the first instance in which the Gouy phase shift is explicitly used to provide destructive interference between two arms of an interferometer. Using this method, the depth resolution can be enhanced by more than an order of magnitude [12].

A schematic of the interferometer is shown in Fig. 1. This spectrometer shares many features with terahertz imaging systems described earlier [13], [14]. The terahertz pulses are generated and detected using low-temperature-grown GaAs photoconductive antennas, gated with 50-fs laser pulses from a mode-

Manuscript received January 18, 2001; revised June 19, 2001. This work was supported in part by the National Science Foundation and in part by the Environmental Protection Agency.

The authors are with the Electrical and Computer Engineering Department, Rice University Houston, TX 77251 USA (e-mail: daniel@rice.edu).

Publisher Item Identifier S 1077-260X(01)09931-2.

locked Ti:sapphire laser. High-density polyethylene lenses are used to collimate, focus, and collect the THz beam, which is arranged in a Michelson configuration for reflection imaging [5]. A high-resistivity silicon wafer is used as a beam splitter, dividing the pulse train into a sample and a reference arm. This wafer is 0.5 cm thick, so that multiple reflections within the beam splitter are delayed by over 150 ps relative to the initial THz pulse, and are not measured. We note that this is not a 50/50 beam splitter—in fact, the transmitted THz field is reduced by a factor of 0.82 relative to the field incident on the silicon wafer, while the THz field reflected from the front surface of the wafer is reduced by a factor of 0.42. However, in the configuration shown in Fig. 1, an ideal 50/50 split is not required, since both the sample arm and the reference arm pulses experience one transmission and one front-surface reflection from the wafer. Thus, both fields are attenuated by a factor of $\sim$0.35 in passing through the interferometer. The imbalance in the two arms is not significant because the interference occurs at the detector, after the two beams have been equalized. The achromaticity and low absorptivity of high-resistivity silicon are more important considerations in choosing a beam-splitter material [15].

A lens is placed in the sample arm of the interferometer, and the sample to be imaged is located at its focus. For imaging, samples can be scanned in the focal spot, transverse to the propagation direction of the THz beam so that an image is acquired pixel by pixel [13], [14], [16]. The beam in the second arm of the interferometer (the reference arm) is simply retro-reflected off of a flat mirror on a manual translation stage. The optical delays of the two arms are adjusted to be approximately equal.

In addition to providing lateral spatial resolution for imaging, the lens also provides the phase shift that permits background-free imaging. The pulse that passes through the lens acquires an additional phase (compared to the pulse that traverses the reference arm) as a result of the Gouy phase shift acquired by a focused Gaussian beam [7], [17]. This topological phase is a result of the variation in wavefront curvature as the pulse passes through the focus, and is approximately equal to π. Thus, when the pulses from the two arms of the interferometer reach the detector, they destructively interfere and a very small signal is measured. However, if the sample contains any feature that distorts either the amplitude or phase of the reflected THz pulse, this destructive interference is disrupted and a large signal is measured. In a sample containing multiple layers, the delay of the reference arm can be adjusted so as to cancel any one of the reflections from the sample, permitting a detailed study of any particular buried interface. Depending on the surface that is generating the reflection in the sample arm, it may be necessary to place an aperture in the reference arm in order to adjust the relative amplitudes of the two pulses.

Fig. 2 shows several terahertz waveforms that illustrate this destructive interference. Fig. 2(a) shows waveforms from the sample arm and reference arm, with a metal mirror placed in the focus of the imaging lens, at the position normally occupied by the sample. These waveforms illustrate the nearly π phase shift acquired by the sample arm, relative to the reference arm. The bottom waveform in Fig. 2(a) shows the strong destructive interference between these two pulses, resulting in a signal reduced in amplitude by more than 90%. The spectra in Fig. 2(b)

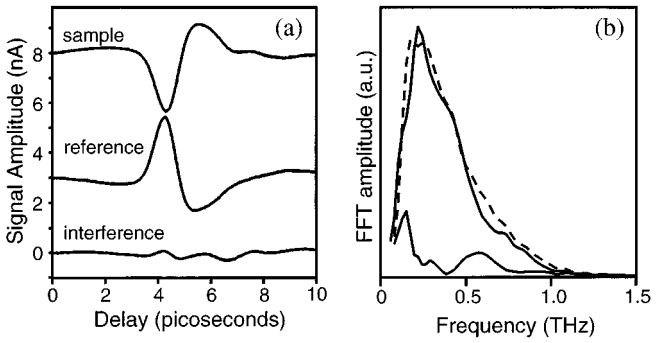

Fig. 2. Sample waveforms and Fourier spectra demonstrating the destructive interference arising from the Gouy phase shift. (a) The waveforms measured in the sample and reference arm alone, when the sample has been replaced by a mirror. These two waveforms are nearly π out of phase. The third waveform illustrates the nearly complete destructive interference of the first two waveforms, when both arms of the interferometer are unblocked. (b) The Fourier spectra (amplitude) of the waveforms in (a). The dashed curve shows the reference waveform, while the larger solid curve shows the waveform from the sample arm. The small solid curve is the spectrum of the interfered waveform. In (a), the waveforms have been vertically offset for clarity.

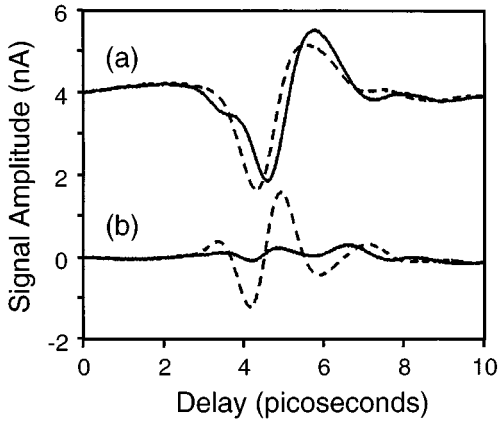

Fig. 3. An illustration of the enhanced contrast provided by interferometry. (a) A comparison of two waveforms from the sample arm alone. The solid curve is reflected from a mirror, while for the dashed curve, a piece of adhesive tape has been affixed to the face of the mirror. (b) The same comparison as in (a), except that the reference arm is unblocked so that the reference pulse can interfere with the sample pulse. The reference pulse delay was adjusted to optimally cancel the sample pulse before the adhesive tape was placed on the mirror. The larger difference between the two waveforms in (b) illustrates the enhanced contrast provided by the nearly background-free measurement. The waveforms in (a) have been vertically offset for clarity.

show the Fourier amplitudes of these three waveforms, with the reference spectrum shown as a dashed curve. As expected, the signal and reference waveforms have very similar spectra, with small differences arising from the weak absorption and dispersion in the thin polyethylene imaging lens or from slight aberrations arising from misalignment. The spectrum of the interfered signal is much weaker, showing only a small low-frequency remnant.

Fig. 3 shows waveforms that illustrate some of the advantages of using this destructive interference in the detection of subtle features in a sample. Fig. 3(a) shows two waveforms acquired with the reference arm blocked. The solid curve represents the waveform reflected from a metal mirror at the focus of the imaging lens, as above. The dashed curve shows the same situation, except that a piece of adhesive tape (approximately

75 μm thick) is affixed to the front of this mirror, covering the THz beam spot. This thin, low-dielectric material introduces a small phase shift and a slight decrease in amplitude. Fig. 3(b) illustrates the same comparison, except that the reference arm of the interferometer is unblocked. Here, the disruption of the destructive interference is much more dramatic. This results primarily from the small change in propagation delay introduced by the insertion of the thin dielectric film and produces a waveform that resembles the derivative of the waveform shown in Fig. 3(a).

The use of interferometry affords several advantages in the detection of subtle features in a sample. First, the fractional change in peak-to-peak amplitude is much larger with interferometry, as shown in Fig. 3. This provides both an increased contrast in the imaging of dielectric discontinuities and an enhanced sensitivity for the detection of sub-coherence-length layers, as demonstrated further below. For the measurements shown in Fig. 3, the coherence length of the THz pulse in free space is about 0.3 mm. In this case, $L_c/2$ in the material is about 40% larger than the thickness of the adhesive tape used in this illustrative example. However, it is clear that the contrast is quite large in this demonstration, and that much thinner features could be detected. Interferometry also provides a background-free method for waveform acquisition, which naturally eliminates common-mode noise arising from laser fluctuations or other external perturbations. Unlike an interferometer for visible light, a THz interferometer does not require submicrometer stability, and is thus far less sensitive to vibrations. Finally, it is compatible with existing THz–TDS techniques, requiring only an additional thick silicon beam splitter and a mirror.

We note that previous THz imaging experiments have demonstrated a high degree of sensitivity to small shifts in the delay of a measured pulse [14]. The interferometric technique converts these delay shifts into amplitude shifts as follows. Consider one frequency component of frequency ω in the reference arm of the interferometer, which can be described as $E_R = e^{i\omega t}$. The corresponding component of the sample arm waveform, with a π phase shift, may be written as $E_S = -e^{i\omega t}e^{i\phi}$. Here, $\phi = 2D\omega/c$ is the phase delay associated with the displacement of the reflecting surface in the sample arm, relative to zero optical path mismatch. We assume that D is much smaller than the confocal parameter of the focusing beam. The superposition of these two signals is $2i\sin(\phi/2)\cdot e^{i\omega t}e^{i\phi/2}$. In the limit of small displacement D, the amplitude of the interference signal is modulated by a factor of ϕ. Thus, small changes in the phase of the sample arm wave lead to equivalent small changes in the amplitude of the interfered wave.

We note that the signal resulting from the interference of the two pulses is not quite zero even when the sample and reference reflectors are identical (see Fig. 2). We can understand this incomplete destructive interference as a manifestation of the frequency dependence of the Gouy phase. The additional phase shift acquired by a focusing Gaussian beam is given by

$$\Delta\Phi_G(\nu) = \pi - 2\cdot\tan^{-1}\left(\frac{2\nu_c}{\pi\nu}\right) \tag{1}$$

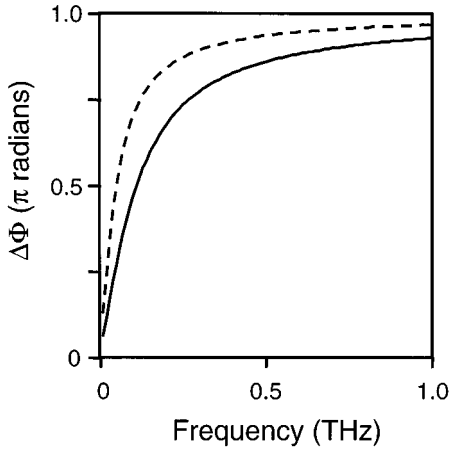

Fig. 4. The phase difference between the sample and reference arms resulting from the Gouy phase, calculated using (1). The solid line shows $\Delta\Phi_G(\nu)$ for $\nu_c = 176$ GHz, while the dashed line shows the result for $\nu_c = 80$ GHz. These values are typical for the experimental configurations used in this paper.

where $\nu_c = fc/w_0^2$, f is the focal length of the lens, and w_o is the beam waist before the lens [7]. For frequencies larger than the critical frequency ν_c, the Gouy phase shift approaches π, but for lower frequencies, the confocal parameter of the focusing beam approaches the focal length of the lens and the phase shift rapidly drops to zero. For a typical experimental configuration, with a lens with $f = 13.2$ cm, we estimate a beam waist of 1.5 cm and thus a critical frequency of $\nu_c = 176$ GHz. Fig. 4 shows the frequency dependence of the phase difference $\Delta\phi_G$ for two values of ν_c, including this value. From a comparison of this plot with Fig. 2(b), it is clear that a phase shift of π is not expected for all the wavelengths in the THz pulse. As a result, the interference between the sample and reference arms is not complete, particularly at low frequencies. The amplitude of this residual waveform depends on the parameters of the optical configuration such as the lens focal length and also on the bandwidth of the incident THz pulse.

We can confirm that this incomplete cancellation is responsible for the observed waveforms by measuring the interfered waveforms as a function of the delay between the sample and reference arms. In this case as above, both arms are retro-reflected with identical metal mirrors. In Fig. 5, we compare these measured waveforms (solid curves) with simulated data (dashed curves). For these simulations, we measure the reference arm pulse $E_{\rm ref}(t)$ with the sample arm blocked. We then compute the sum of this reference pulse and a delayed, phase-shifted replica of itself. That is, we plot the inverse Fourier transform of

$$E_{\rm ref}(\omega)\left[1 + e^{-i2\omega D/c}\,e^{i\Delta\Phi_G(\omega)}\right] \tag{2}$$

for each position of the reference arm delay line. Here, $E_{\rm ref}(\omega)$ is the Fourier transform of $E_{\rm ref}(t)$ and D is the displacement of the reference arm mirror. This simulates the coherent superposition of the reference and sample arm waveforms, using only the reference arm waveform as an input. The excellent agreement between the measurements and simulations indicates that the Gouy phase is sufficient to explain the observed waveforms.

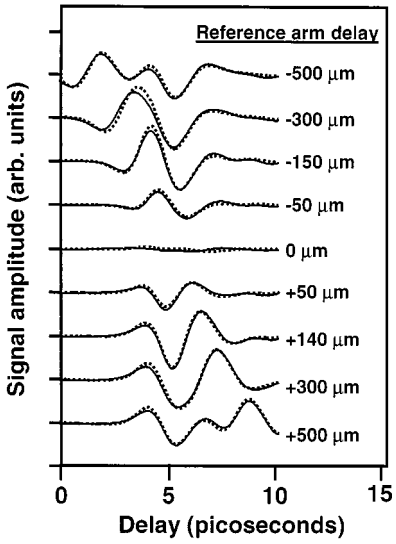

Fig. 5. The solid lines show a series of interfered waveforms, measured for different values of the displacement of the retro-reflecting mirror in the reference arm. The dashed lines are simulated waveforms, using a measured reference arm waveform and the Gouy phase calculated from (1), as described in the text. The excellent agreement indicates that the Gouy phase is sufficient to explain the observed waveforms.

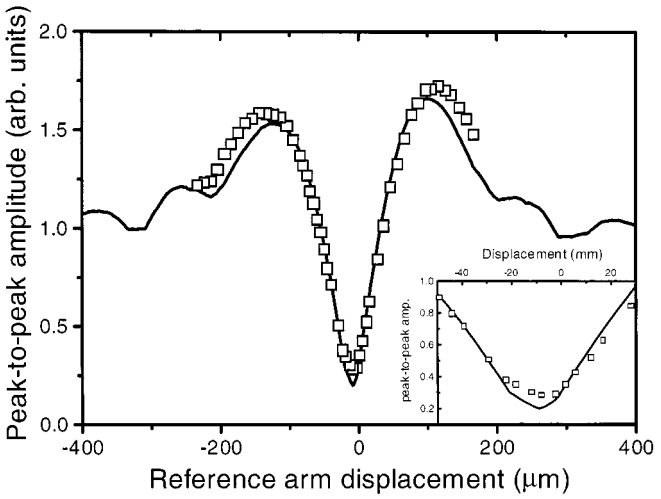

Fig. 6. The peak-to-peak amplitude of the measured waveforms as a function of the displacement of the reference arm mirror. Open squares are experimental data points. The solid line is simulated using a measured reference arm waveform and the Gouy phase calculated from (1), as described in the text. The peak contrast $C_{\rm peak}$ for these data is about five. The coherence length of the pulse used in these measurements is $\sim$200 μm, but the variation in the peak-to-peak amplitude is linear to within $\sim$10 μm of its minimum value. This can be seen in the inset, which is an expanded view of the portion of the data near zero displacement.

Fig. 6 shows a simple metric for this single-cycle pulse interference effect. It displays the peak-to-peak amplitude of both the experimental and the simulated waveforms as a function of the delay of the reference arm. This plot shows the destructive interference near zero delay, as well as constructive interference on either side of zero delay. The solid curve shows the peak-to-peak amplitudes of the simulated waveforms, calculated as described above with the measured reference arm waveform as an input. For these measurements, the coherence length $L_c \sim 200$ μm and the critical frequency $\nu_{\rm c} \sim 80$ GHz. Although the amplitude is not zero at zero delay, it is almost an order of magnitude less than at maximum constructive interference. Also, the amplitude variation is roughly contained within a displacement range of $D = \pm L_c/2$, and it is roughly proportional to D to within $\sim$10 μm of its minimum value. This can be seen in the inset, which is an expanded view of the portion of the data near zero displacement. This illustrates how interferometry provides a large dynamic range for the conversion of small shifts in delay into large amplitude variations.

The behavior of the amplitude of the interfered waveform is further illustrated in Fig. 7, which shows a calculation of peak-to-peak waveform amplitude as a function of the reference arm delay for three different pulse coherence lengths. These simulations use a model single-cycle pulse as an input (the first derivative of a Gaussian) and assume a critical frequency of $\nu_c = 0.1$ THz. With decreasing THz bandwidth, the optimal cancellation degrades, resulting in a smaller contrast between the minimum and maximum amplitudes. It is also interesting to note an increasing asymmetry relative to zero delay, which results from the increasingly severe (and asymmetric) distortion of the single-cycle pulse by the frequency-dependent Gouy phase.

To parameterize the degree of contrast enhancement, we define the peak contrast $C_{\rm peak}$ as the ratio of the peak-to-peak amplitude at large displacement (when the two waveforms are well separated) to the minimum peak-to-peak amplitude (when the destructive interference is optimized). This provides a useful measure of the expected enhancement in both contrast and detectability. If the Gouy phase were exactly equal to π at all frequencies, then the two waveforms would precisely cancel at $D = 0$, and $C_{\rm peak}$ would be infinite. The inset in Fig. 7 shows

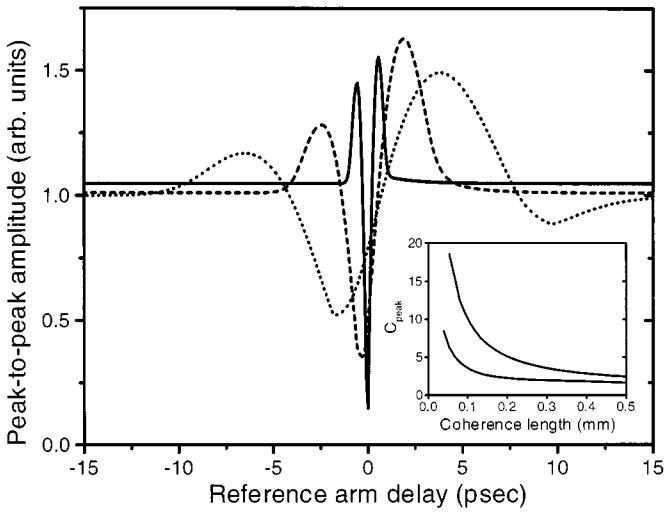

Fig. 7. Simulations of the peak-to-peak waveform amplitude as a function of the reference arm delay for three different pulse coherence lengths. These simulations use a model single-cycle pulse (the first derivative of a Gaussian) as the input pulse. The coherence length is varied by changing the temporal width of the Gaussian. To implement the Gouy phase shift, (1) is used, with a critical frequency of $\nu_c = 100$ GHz assumed. The solid line is for $L_c = 100$ μm, the dashed line is for $L_c = 400$ μm, and the dotted line is for $L_c = 1$ mm. The inset shows the peak contrast $C_{\rm peak}$, defined as the ratio of the peak-to-peak amplitude at large displacement to the minimum peak-to-peak amplitude, as a function of the input pulse coherence length. The upper curve is the result for $\nu_c = 100$ GHz, while the lower curve is for $\nu_c = 300$ GHz.

C_{peak} as a function of the pulse coherence length for two different values of ν_c. It is clear that broader bandwidths can significantly enhance the contrast. However, it is interesting to note that an order of magnitude contrast enhancement can be obtained with even a relatively modest bandwidth of $\sim$1 THz, corresponding to a coherence length in free space of $\sim$100 μm.

To quantitatively assess these improvements, it is necessary to compute the coherence length of the pulses used in the measurements. For the simulated pulses used to generate Fig. 7, this calculation is straightforward, but for experimentally generated pulses some subtleties arise. Normally, the coherence time τ_c of a light source is defined as the standard deviation of $|\Gamma^{(1)}(\tau)|^2$

$$\tau_c^2 = \int (\tau - \langle\tau\rangle)^2 \left|\Gamma^{(1)}(\tau)\right|^2 d\tau \Big/ \int \left|\Gamma^{(1)}(\tau)\right|^2 d\tau \tag{3}$$

where $\Gamma^{(1)}(\tau)$ is the first-order coherence function

$$\Gamma^{(1)}(\tau) = \int E(t-\tau)\cdot E(t)\,dt. \tag{4}$$

Since $\Gamma^{(1)}(\tau)$ is symmetric with respect to τ, the average value $\langle\tau\rangle$ in (3) vanishes. Because $\Gamma^{(1)}(\tau)$ is the Fourier transform of the power spectrum, one may formulate an alternative definition for τ_c in terms of the spectral bandwidth

$$\tau_c = \frac{1}{\pi\cdot\Delta\nu} \tag{5}$$

where $\Delta\nu$ is the full width at $1/e$ of the power spectrum. Once the coherence time is determined, the coherence length is computed using $L_c = c\tau_c/n$, where n is the refractive index of the medium in which the radiation propagates [18].

In many cases, these two formulations are equivalent. However, in the case of interest here, a typical THz pulse consists not only of a single-cycle oscillation but also of a subsequent train of smaller oscillations. This temporal structure is entirely repeatable and is not due to noise in the measurement. Rather, it can arise from the effects of water vapor absorption in the THz beam path or from temporal echoes arising from either optical or electrical reflections in the transmitter or receiver antenna [19]. In either case, the presence of this structure following the main THz pulse mimics the effect of a narrow-band component within the pulse spectrum. As a result, the coherence time is artificially lengthened if this extended temporal structure is included in the computation. This is demonstrated in Fig. 8, which shows a typical THz waveform along with the coherence length calculated using the two methods outlined above. This waveform has been measured within a purged container, so that the effects of water vapor are minimized; even so, considerable structure follows the main pulse. In the calculation of the coherence length, this time-domain waveform is numerically truncated using a square window function with tapered rising and falling edges, and the coherence length is calculated as a function of the location of the falling edge of the window. The rising edge is kept fixed at $\tau = -5$ ps, well before the beginning of the pulse. The dashed line, calculated with the method of (3) and (4), shows a large increase in the computed coherence length each time the window function broadens to encompass one of the small echoes that follow the main pulse. The coherence length calculated using

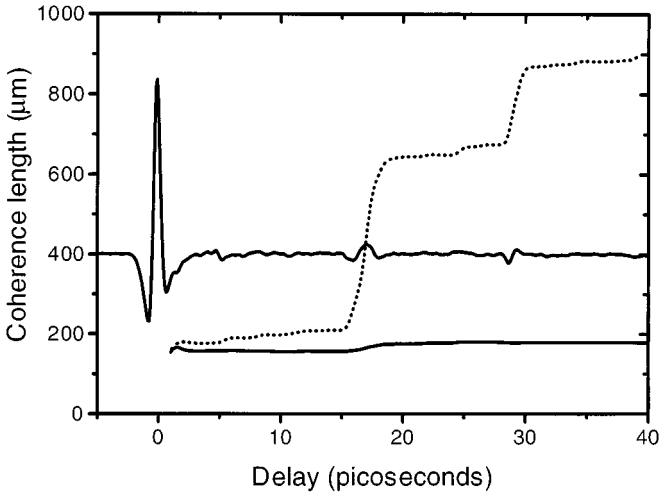

Fig. 8. A typical waveform (in arbitrary units) superimposed on calculations of its coherence length using the two methods described in the text. To perform these calculations, the waveform is multiplied by a window function with rounded rising and falling edges. The rising edge is kept fixed at $\tau = -5$ ps, well before the start of the pulse. The coherence length is calculated as a function of the position of the falling edge, which is varied from 1 to 40 ps. The dashed curve shows the computation based on (3) and (4), while the nearly flat solid curve shows the results from (5). The former method is much more sensitive to the secondary structure that follows the main transient and can produce misleading results.

the full waveform is 900 μm, nearly six times larger than the value calculated with only the initial single-cycle transient. In contrast, since the small structures at large values of the delay do not dramatically change the shape of the spectrum, the value of L_c calculated using (5) (solid line) is much less sensitive to the width of the window function. Of course, the coherence properties of the radiation necessarily include the full time dependence of the THz electric field and are correctly characterized using (3) and (4), along with higher order coherence functions. However, for the purposes of determining the depth resolution in time-of-flight measurements such as those described here, only the coherence of the initial portion of the waveform is relevant. To accurately extract a measure of the Rayleigh limit in such imaging experiments, the inverse spectral bandwidth is a more reliable measure than the width of $\Gamma^{(1)}(\tau)$. The relevant coherence length can be defined to be the limiting value as the width of the window function shrinks to include only the initial transient.

To demonstrate the ability to image below the coherence limit, we have constructed several model samples containing thin, well-controlled features. Fig. 9 shows a schematic of one Teflon–metal model, with air gaps between the two pieces ranging from 12.5 to 100 μm in width. This model is positioned so that the metal–plastic interface is located at the focus of the imaging lens in the sample arm. We carefully adjust the tilt of the sample so that, as it is scanned transverse to the beam propagation direction, the distance from the lens to this interface does not vary. We image a line scan across this sample and compare the results with and without the interferometric cancellation. In Fig. 10, we show the percent change in the peak-to-peak amplitude of the measured waveform relative to a waveform measured at a position on the sample containing no air gap. For these measurements, the delay of the reference

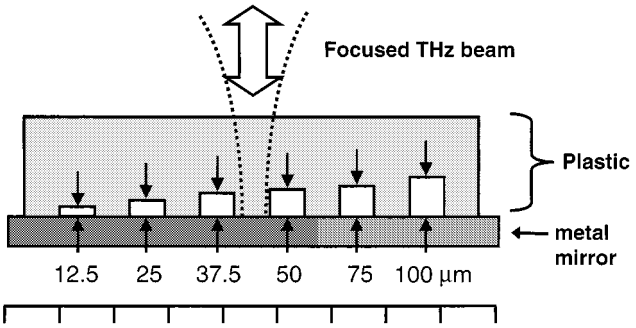

Fig. 9. A schematic cross-section of one of the model samples used to compare the resolution limit of the interferometric and noninterferometric imaging. The scale bar at the bottom of the figure shows a tick mark every 10 mm.

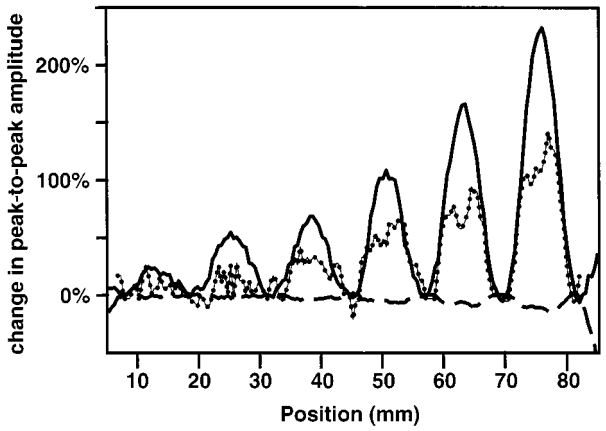

Fig. 10. Line scan images of the sample shown in Fig. 9. These show the change in peak-to-peak amplitude of the waveform, relative to a waveform measured at a position where there is no air gap, as a function of position along a line across the sample, slicing through the six air gaps. The solid curve shows the result when interferometry is employed, while the dashed curve shows the result without interferometry. The dotted curve is the noninterferometric result multiplied by -10, shown to facilitate comparison with the interferometric result. The widths of the air gaps are as labeled in Fig. 9. In these measurements, the coherence length of the radiation was $\sim$315 μm.

arm has been used to optimize the cancellation of the pulse reflected from the metal–plastic interface, with no air gap in the beam. As seen in Fig. 3, the waveform increases in amplitude when interferometry is employed but decreases when it is not. More importantly, the contrast of the interferometric signal is enhanced by more than an order of magnitude over the noninterferometric signal. In the interferometric mode, the areas with no air gap show strong destructive interference. The change in the cancellation when an air gap is encountered results in a large increase in the amplitude of the measured waveform. As a result, it is possible to easily detect the smallest air gap using the interference effect. This 12.5-μm gap is roughly 25 times smaller than the coherence length of the terahertz pulses used to collect this data.

As mentioned above, the results of Fig. 10 for the amplitude modulation of the interferometric waveform should be equivalent to the phase modulation of the sample arm alone, with the reference arm blocked. For the purposes of this comparison, we extract the phase of the measured sample arm waveforms at one particular frequency. This result is normalized and displayed in Fig. 11, along with the interferometric result of

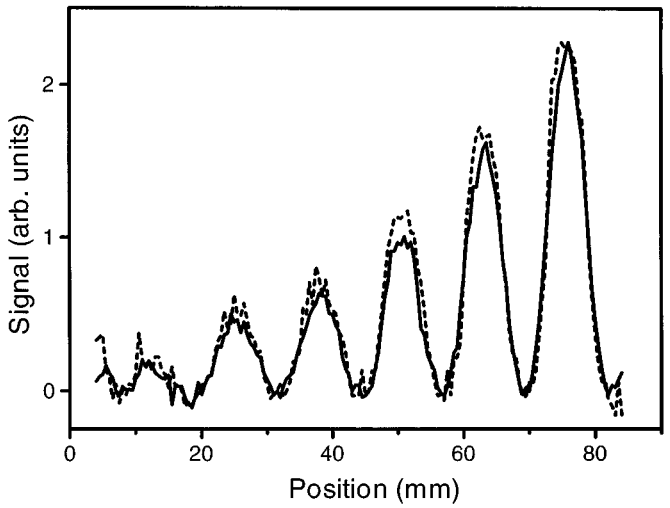

Fig. 11. Line scan images of the sample shown in Fig. 9. The solid curve shows the same result as the solid curve in Fig. 10, which is the peak-to-peak amplitude of the interferometric signal. The dashed curve shows variation in phase of the sample arm waveforms, measured without interferometry. These data correspond to the phase measured at one particular frequency in the pulse spectrum, $\nu = 0.5$ THz. These curves have been normalized so that their maxima are equal. As described in the text, these results show very similar dependence on the width of the air gap.

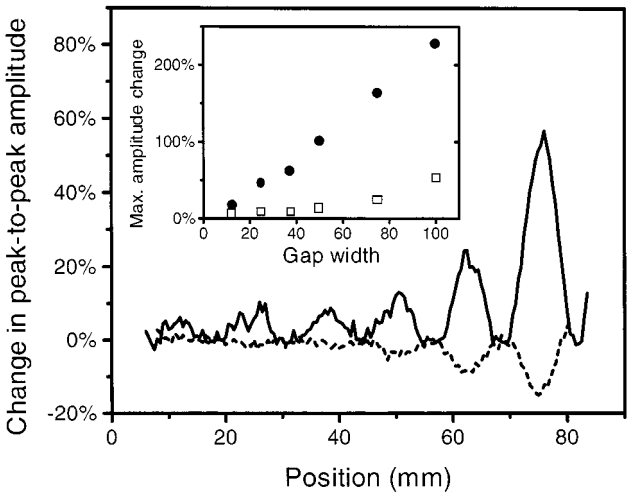

Fig. 12. Line scan images of the sample shown in Fig. 9. As in Fig. 10, these show the change in peak-to-peak amplitude of the waveform, relative to a waveform measured at a position where there is no air gap, as a function of position along a line across the sample. The solid curve shows the result when interferometry is employed, while the dashed curve shows the result without interferometry. In these measurements, the coherence length of the radiation was $\sim$525 μm. The inset shows the maximum change in pulse amplitude for each of the six different air gaps, for the interferometric data from Figs. 10 (short coherence length, solid circles) and 12 (long coherence length, open squares).

Fig. 10. As expected, the degrees of modulation for these two methods are quite comparable, although the phase results are somewhat noisier.

As one would expect, the degree of modulation depends on the bandwidth of the THz pulse used to collect the data. Fig. 12 shows data similar to that of Fig. 10, except that a different set of photoconductive antennas have been used to generate and detect the THz radiation. In this case, the coherence length is substantially longer, $L_c \sim 525$ μm. The increase in sensitivity

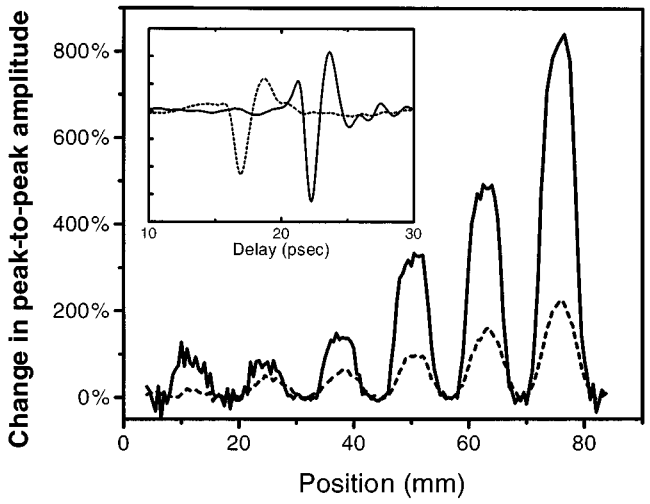

Fig. 13. Line scan images, similar to those shown in Figs. 10–12. Here, two interferometric line scans are compared. These were acquired using the two reference waveforms shown in the inset. For the dashed curves, the coherence length was 345 μm and the spectrum-weighted average frequency of the pulse was 250 GHz. For the solid curves, the coherence length was quite similar, but the average frequency was 40% larger. This leads to an enhancement in the signal contrast because of the frequency-dependence of the Gouy phase.

to small gaps resulting from the interferometric measurement is much smaller in this case, as a result of two factors. First, it is more difficult to measure thin features with a longer coherence length, because of the Rayleigh criterion. Second, the lower bandwidth used in this measurement leads to a less effective destructive interference between the sample and reference pulses, since the Gouy phase is far from π over a substantial portion of the bandwidth. As shown in Fig. 7, this leads to a smaller available contrast range. The inset shows the maximum change in the peak-to-peak amplitude for the six air gaps, as a function of gap width, for the two interferometric line scans shown in Figs. 10 (solid circles) and 12 (open squares). If the bandwidth is broad enough, then the variation in peak-to-peak amplitude is nearly linear with the gap width, but for narrower bandwidth pulses, these data depart from linearity. These results are consistent with the simulations shown in Fig. 7, in which longer coherence lengths lead to more distorted contrast curves.

Ordinarily, one would expect the depth resolution in a time-of-flight measurement to be determined by the bandwidth of the radiation and to be only weakly dependent on its central frequency. For example, for a light source with a Gaussian spectrum, the coherence time is simply $1/4\pi\sigma_\nu$, where σ_ν is the standard deviation of the squared power spectrum [18]. However, because of the frequency dependence of the Gouy phase, the center frequency can also play a role in these measurements. Fig. 13 shows two line scans, both representing the peak-to-peak amplitudes of the interfered waveforms. As in Fig. 12, different sets of antennas have been used to collect these two scans. The inset shows the two different reference arm waveforms used to acquire these two line scans. These two pulses have comparable bandwidths and therefore coherence lengths, but the spectrum-weighted mean frequency of the solid curve is ~40% larger than that of the dashed curve. Because the central frequency is shifted to higher values, the Gouy phase difference is closer to π for most of the frequency content of this waveform, so the destructive interference between sample and reference pulses is more effective. As a result, even though the coherence lengths are quite similar, the pulse with a higher average frequency gives a substantially enhanced contrast in imaging the sample. Using the waveform with the higher central frequency, we observe that the waveform nearly doubles in amplitude in the vicinity of the smallest, 12.5-μm gap.

As a final point, it is worth mentioning the role of the transverse spatial resolution in these data. The features shown in the sample of Fig. 9 are all much thinner than the Rayleigh range of the focused THz beam, even for its highest frequency components, so it is reasonable to neglect wavefront curvature in these experiments. This effectively decouples the considerations of transverse and longitudinal resolution in an imaging measurement. However, it is important to remember that different frequency components focus to different spot sizes, so the focal spot of this broadband light source is quite complicated. Since we are relying on a time-domain metric (the peak-to-peak amplitude of the temporal waveform) for formation of images, the expected transverse resolution is not so easy to determine. One might guess that it would vary approximately linearly with the central frequency of the radiation. We extract from the data of Fig. 13 a 10–90% rise for the largest air gap, as a measure of the transverse spatial resolution. We find that the data acquired using the waveform with a higher central frequency gives a transverse resolution of ~2.5 mm, while the lower frequency result is ~3.8 mm, in rough agreement with the shift in the central frequency of the THz pulse. We note that the interferometric technique permits the resolution of features in the longitudinal direction that are more than 100 times smaller than the smallest features that can be resolved in the transverse dimensions.

In conclusion, we have demonstrated a version of optical coherence tomography using single-cycle pulses of THz radiation. Although conceptually quite similar to OCT, the ability to directly detect the electric field of the reflected waveform provides new imaging capabilities beyond those explored in the optical regime. Fig. 5 emphasizes the distinction between THz interferometric imaging and conventional optical coherence tomography. In OCT, data are acquired by interfering two beams (signal and reference) and measuring the intensity of this interfered signal as a function of the delay of the reference arm. This can be expressed simply as

$$S_{\mathrm{OCT}}(\tau) \propto \int dt\, |[E_{sig}(t) + E_{ref}(t+\tau)]|^2 . \qquad (6)$$

Here, τ is the delay of the reference arm and t is the time axis for the electric fields. In contrast, the THz measurements presented here provide a direct measurement of the quantity inside the square brackets in (6), for any chosen value of τ. It is clear that the destructive interference demonstrated in Fig. 2 has also been observed in ultrafast OCT measurements. This effect is manifested as one data point in a temporal interference fringe pattern [1]. It is important to note that the OCT analysis generally requires the measurement of the entire fringe pattern to extract information about the electric field $E_{\mathrm{sig}}(t)$. In the THz experiment, one can measure $E_{\mathrm{sig}}(t)$ without varying the reference arm delay at all. This permits the resolution of features in a sample that are well below the Rayleigh limit imposed

by the bandwidth of the radiation source. Moreover, the technique is entirely general, in the sense that the Gouy phase is a purely geometrical effect applicable to any focused electromagnetic wave. Thus one might hope that with recent advances in femtosecond pulse measurement techniques [20], the ability to obtain sub-coherence-length images could eventually be implemented at higher frequencies.

REFERENCES

[1] D. Huang, E. A. Swanson, C. P. Lin, J. S. Schuman, W. G. Stinson, W. Chang, M. R. Hee, T. Flotte, K. Gregory, C. A. Puliafito, and J. G. Fujimoto, "Optical coherence tomography," *Science*, vol. 254, pp. 1178–1181, 1991.

[2] M. R. Hee, J. A. Izatt, E. A. Swanson, and J. G. Fujimoto, "Femtosecond transillumination tomography in thick tissues," *Opt. Lett.*, vol. 18, pp. 1107–1109, 1993.

[3] Y. Pan, R. Birngruber, J. Rosperich, and R. Engelhardt, "Low-coherence optical tomography in turbid tissue: Theoretical analysis," *Appl. Opt.*, vol. 34, pp. 6564–6574, 1995.

[4] D. Huang, J. Wang, C. P. Lin, C. A. Puliafito, and J. G. Fujimoto, "Micron-resolution of cornea anterior chamber by optical reflectometry," *Lasers Surg. Med.*, vol. 11, pp. 419–425, 1991.

[5] D. M. Mittleman, S. Hunsche, L. Boivin, and M. C. Nuss, "T-ray tomography," *Opt. Lett.*, vol. 22, pp. 904–906, 1997.

[6] P. R. Smith, D. H. Auston, and M. C. Nuss, "Subpicosecond photoconducting dipole antennas," *IEEE J. Quantum Electron.*, vol. 24, pp. 255–260, 1988.

[7] A. B. Ruffin, J. V. Rudd, J. F. Whitaker, S. Feng, and H. G. Winful, "Direct observation of the Gouy phase shift with single-cycle terahertz pulses," *Phys. Rev. Lett.*, vol. 83, pp. 3410–3413, 1999.

[8] F. V. Kowalski, W. T. Hill, and A. L. Schalow, "Saturated-interference spectroscopy," *Opt. Lett.*, vol. 2, pp. 112–114, 1978.

[9] M. D. Levenson and G. L. Eesley, "Polarization selective optical heterodyne detection for dramatically improved sensitivity in laser spectroscopy," *Appl. Phys.*, vol. 19, pp. 1–17, 1979.

[10] R. Oldfield, *Light Microscopy: An Illustrated Guide*. London, U.K.: Wolfe, 1994, pp. 95–103.

[11] T. van Kessel and H. K. Wickramasinghe, "Measurement of trench depth by infrared interferometry," *Opt. Lett.*, vol. 24, pp. 1702–1704, 1999.

[12] J. L. Johnson, T. D. Dorney, and D. M. Mittleman, "Enhanced depth resolution in terahertz imaging using phase-shift interferometry," *Appl. Phys. Lett.*, vol. 78, pp. 835–837, 2001.

[13] B. B. Hu and M. C. Nuss, "Imaging with terahertz waves," *Opt. Lett.*, vol. 20, pp. 1716–1719, 1995.

[14] D. M. Mittleman, R. H. Jacobsen, and M. C. Nuss, "T-ray imaging," *IEEE J. Select. Topics Quantum Electron.*, vol. 2, pp. 679–692, 1996.

[15] D. Grischkowsky, S. Keiding, M. van Exter, and C. Fattinger, "Far-infrared time-domain spectroscopy with terahertz beams of dielectrics and semiconductors," *J. Opt. Soc. Amer. B*, vol. 7, pp. 2006–2015, 1990.

[16] D. M. Mittleman, M. Gupta, R. Neelamani, R. G. Baraniuk, J. V. Rudd, and M. Koch, "Recent advances in terahertz imaging," *Appl. Phys. B*, vol. 68, pp. 1085–1094, 1999.

[17] A. E. Siegman, *Lasers*. Mill Valley, CA: University Science, 1986.

[18] O. Svelto, *Principles of Lasers*, 4th ed. New York: Plenum, 1998.

[19] M. van Exter, C. Fattinger, and D. Grischkowsky, "Terahertz time-domain spectroscopy of water vapor," *Opt. Lett.*, vol. 14, pp. 1128–1130, 1989.

[20] A. Baltuska, M. S. Pshenichnikov, and D. A. Wiersma, "Second-harmonic generation frequency-resolved optical gating in the single-cycle regime," *IEEE J. Quantum Electron.*, vol. 35, pp. 459–478, 1999.

Jon L. Johnson, photograph and biography not available at the time of publication.

Timothy D. Dorney received the B.S. degree in electrical engineering from Texas A&M University, College Station, in 1990 and the M.S. degree in electrical engineering and applied physics from Case Western Reserve University, Cleveland, OH, in 1992. He is currently pursuing the Ph.D. degree in electrical and computer engineering at Rice University, Houston, TX. He has ten years of experience in VLSI design working on variou DRAM projects at Texas Instruments. He currently holds six patents and several pending patents. His most recent research involves digital signal processing, material parameter estimation, and imaging with terahertz time-domain signals

Daniel M. Mittlemen received the B.S. degree from the Massachusetts Institute of Technology, Cambridge, MA, and the Ph.D. degree from the University of California, Berkley, both in physics.

He spent two years as a Postdoctoral Researcher at Bell Laboratories, working on the development of terahertz "T-ray" imaging. He has been in the Electrical and Computer Engineering Department, Rice University, Houston, TX, since 1996. His research interests include terahertz imaging and spectroscopy and the study of photonic crystals at both visible and terahertz frequencies.